CONF-921103--6

UCRL-JC-111286
PREPRINT

Laser Driven Hydrodynamic Instability Experiments

B. A. Remington, S. V. Weber, S. W. Haan, J. D. Kilkenny,
S. G. Glendinning, R. J. Wallace, W. H. Goldstein,
B. G. Wilson, and J. K. Nash

This paper was prepared for submittal to the 34th Annual
APS Meeting of the Division of Plasma Physics
November 16-20, 1992, Seattle, WA

December 7, 1992

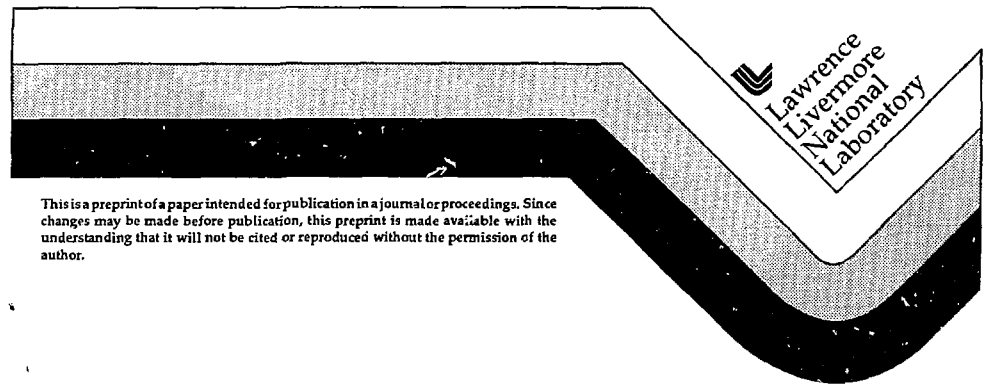

UCRL-JC--111286

DE93 005822

Laser Driven Hydrodynamic Instability Experiments

B.A. Remington, S.V. Weber, S.W. Haan, J.D. Kilkenny, S.G. Glendinning, R.J. Wallace, W.H. Goldstein, B.G. Wilson, and J.K. Nash

Lawrence Livermore National Laboratory
Livermore, CA 94550

ABSTRACT

We have conducted an extensive series of experiments on the Nova laser to measure hydrodynamic instabilities in planar foils accelerated by x-ray ablation. Single mode experiments allow a measurement of the fundamental growth rates from the linear well into the nonlinear regime; multimode foils allow an assessment of the degree of mode coupling; and surface-finish experiments allow a measurement of the evolution of a broad spectrum of random initial modes. Experimental results and comparisons with theory and simulations are presented.

PACS 52.35.Py, 52.70.-m, 52.65.+z

I. INTRODUCTION

The configuration of a high density fluid sitting on top of a low density fluid is Rayleigh-Taylor[1] unstable. Random perturbations at the interface between the two fluids will grow, with fingers (or "spikes") of the heavier fluid poking through the lighter fluid, and bubbles of the lighter fluid rising into the heavier fluid. A good overview of the Rayleigh-Taylor (RT) instability is contained in Ref. 2. The density mismatch between the fluids, expressed with the Atwood number $A = (\rho_1-\rho_2)/(\rho_1+\rho_2)$, determines whether a clean interchange occurs or whether Kelvin-Helmholtz[3] (KH) swirling due to the shears generated during penetration leads to turbulence and subsequent mixing of the fluids. This combination of the RT instability, its shock-driven analogue the Richtmyer-Meshkov[4] (RM) instability, and the KH instability is found in a diverse range of fields spanning nuclear physics to astrophysics. A most spectacular occurrence of the RT instability appears in recent modeling of supernova, where RT-induced mix is invoked to explain degraded light emission curves.[5] The RT instability, alternatively referred to as the fluid interchange instability, appears in other areas of astrophysics as well, such as models of neutron stars,[6] and the sun.[7] Another intriguing recent occurrence of the RT instability is in modeling of multifragmentation in heavy-ion nuclear collisions.[8] Given the endpoints of cosmological and nuclear scales, there is ample room in between for other occurrences of the RT instability. Such areas include atmospheric physics[9] (a specific example being the *barium-release experiment*[10]), *geophysics*,[11] *Z-pinches*,[12] tokamaks,[13] situations where plasmas are confined by magnetic fields in general,[14] and inertial confinement fusion (ICF).[15] A study of the RT instability under conditions relevant to laser-driven ICF is the subject of this paper.

The basic mechanism of driving an implosion by ablating the outer layers of a spherical capsule is inherently RT unstable, independent of the details of the drive. In the accelerating reference frame of the ablation front, the heavy ablator fluid (pusher) is "sitting on top of" the lighter hot, expanding ablated plasma. Perturbations at the ablation front, whether initiated by capsule surface imperfections or by laser hot spots, will grow, possibly leading to shell breakup. Sufficient growth at the ablation front during the acceleration phase can also feed through to seed perturbations at the inner surface. These in turn grow during the deceleration and stagnation stage of the implosion, leading to mixing of the pusher material into the fuel and degraded performance.[15] A simple classical estimate for ideal, incompressible fluids leads to exponential growth of perturbations of amplitude η in the linear regime, $\eta=\eta_0 e^{\gamma_{CI} t}$, where $\gamma_{CI}=(Akg)^{1/2}$, $A = (\rho_1-\rho_2)/(\rho_1+\rho_2)$ is the Atwood number, and $k=2\pi/\lambda$. The expected growth, however, is less due to the combined effects of ablation, finite density gradient, nonlinearities, and compression. Precisely how much less may well determine the ultimate fate of ICF. Thorough, well-diagnosed experiments together with rigorous comparisons with modeling are critical to help guide the design of high performance capsules. A number of experiments have been done in direct drive,[16] that is, where laser light directly illuminates the accelerating surface. Our work is the only active experimental RT effort that we are aware of for indirect drive, where the laser light is first converted to x-rays in a high-Z case called a hohlraum.

We report here on a series of RT experiments with planar foils[17] of fluorosilicone (FS) and CH(Br), using a shaped, low adiabat x-ray drive. Similar shaped drives are called for in high-performance capsule designs to minimize shock heating of the pusher and hence maximize the peak

compression of the implosion. In Sec. II we describe the experimental setup, and in Sec. III we present results from single-mode experiments and simulations. We discuss our multi-mode experiments in Sec. IV, and present an initial set of data from very recent surface-finish experiments in Sec. V. A summary and conclusion is given in Sec. VI. This paper represents a short overview of a very large amount of experimental and theoretical work. As such, most details will have to be referred to past work or deferred to future reports.

II. EXPERIMENTAL SETUP

Surface perturbations are imposed on one side of a 750 μm diameter FS ($SiOC_4H_7F_3$) or CH(Br) foil (specifically, $C_{50}H_{47}Br_{2.7}$) and mounted across a diagnostic hole on the wall of a Au hohlraum with perturbation facing inwards, as illustrated in Fig. 1a. The foil is accelerated as shown schematically in the figure for face-on geometry. Side-on geometry is similar, except with the hohlraum rotated about its axis of symmetry by 90^0. In face-on experiments, the growing modulations in the foil areal density translate to modulations in transmitted backlighter x-rays. In side-on geometry, the foil position is imaged as a shadow in the backlighter x-rays. The one-dimensional (1D) imaging is accomplished either with a streaked 22X magnification Wölter x-ray microscope[18] (the "22X") or with a new 20X magnification streaked-slit imager.[19] Two-dimensional (2D) x-ray imaging is accomplished with a gated x-ray pinhole camera.[20]

The drive was generated by focussing eight 0.351 μm, 2.1 kJ, 3.2 ns Nova[21] beams into a gold cylindrical hohlraum, which then convert to x-rays as shown in Fig. 1a. The drive laser pulses have a low intensity, ~1-ns foot followed by a rapid increase to peak power at ~2.5-3.0 ns, with the ratio (peak intensity)/(foot intensity) = 10-20, as shown in Fig. 1b. This generic

shape is designed to keep the foil on a low isentrope, that is, high compression with a minimum of shock heating. The foil was backlit with a large area spot of x-rays created by irradiating a backlighter disk with a ninth Nova beam of wavelength, shape, and energy of 0.53 μm, 5.0 ns square, and 2.5 kJ, respectively. Depending on the particular experiment, a random phase plate was sometimes used to smooth the backlighter beam.

We show in Fig. 1c a streaked image of a foil trajectory experiment using a CH(Br) foil. This side-on measurement using the streaked-slit imager[19] with Fe x-rays (6.7 keV) tracks the shadow of the foil viewed edge-on. The trajectory deduced from a combination of three such shots,[17] using either the streaked slit or the 22X,[18] is shown in Fig. 1d, along with the results of 1D LASNEX[22] simulations. We achieve a high degree of reproducibility in the data, and the agreement with simulations is excellent, indicating a good overall understanding of the drive and opacity.

III. SINGLE-MODE EXPERIMENTS

To illustrate the basic features of a perturbation growth experiment, we show in Fig. 2a the result of gated x-ray images in side-on geometry of an accelerated FS foil containing a λ = 100 μm, η_0 = 4.5 μm sinusoidal perturbation. Early in time (2.0 ns) the perturbation is still small and sinusoidal, indicating the linear regime of RT growth. At 3.2 ns the foil is quite compressed and the shape of the ablation front is difficult to resolve. By 4.4 ns, the foil has decompressed substantially and evolved into the classic bubble-and-spike shape characteristic of the nonlinear regime. We note the distinct lack of Kelvin-Helmholtz mushrooming in the spike tips. In Fig. 2b, an enlarged version of one of the late-time images is shown, along with isodensity contours from 2D LASNEX simulations in Fig. 2c. The agreement is quite satisfactory, indicating that our modeling and overall

understanding is very good both in the linear regime and in the nonlinear regime. The simulations also indicate no tip broadening in the spikes.

Perturbation growth is more quantitatively studied using face-on radiography, as shown in Fig. 3. A streaked image of a CH(Br) foil containing a sinusoidal initial perturbation is shown in Fig. 3a. Optical depth profiles at early (0.2 ns), intermediate (2.2 ns), and late (4.2 ns) times are shown in Fig. 3b, with their corresponding Fourier coefficients of optical depth modulation given in Fig. 3c. At early and intermediate times, the perturbation is growing but is still sinusoidal, as evidenced by the lack of higher Fourier harmonics at 2.2 ns, which indicates that the RT evolution is in the linear regime. Late in time, the perturbation has evolved into a very clear nonlinear bubble-and-spike shape, reflected in higher Fourier components up to the fifth harmonic appearing. With the transition from the linear to the nonlinear regime, a change in the perturbation growth rate is also expected. In the linear regime the growth is exponential in time ($\eta=\eta_0 e^{\gamma t}$), whereas the asymptotic limit in the nonlinear regime is bubble growth linear in time due to terminal bubble velocity[23] and spike growth quadratic in time due to the spike approaching freefall. High quality measurements of perturbation growth well into the nonlinear regime are somewhat hampered because a large amount of material is packed into a long, very narrow spike. Finite instrumental spatial resolution makes this spike difficult to see, and their inflight alignment relative to the diagnostic could be problematical.

A more rigorous test of modeling is with foils that do not quickly enter the nonlinear regime, so that exponential growth occurs over a reasonably extended period and spike resolution does not dominate the data. We show in Fig. 4a a streaked image of a FS foil with a λ = 50 μm, η_o = 0.8 μm sinusoidal perturbation in face-on geometry. The fundamental Fourier coefficient (corresponding to λ = 50 μm) of optical depth modulation is

shown as a function of time in Fig. 4b, along with the result from 2D LASNEX simulations. Figure 4c is similar only for a CH(Br) foil with a λ = 50 μm, η_o = 0.5 μm initial perturbation. The data have not been corrected for the instrumental MTF, but rather the MTF has been included into the simulations. In an effort to minimize uncertainties in plasma opacities, large lookup tables have been generated using the STA[24] and OPAL[25] opacity models. The two models lead to very similar foil accelerations; for convenience, all calculations shown have used the STA opacities. The simulations are in very good agreement with the data throughout the linear regime and substantially into the nonlinear regime.

To illustrate the subtle differences in the hydrodynamic behavior of the FS versus CH(Br) foils, we plot in Fig. 4d an estimated growth rate, γ, versus perturbation wavelength, λ. To do this we use a simple dispersion formula,[26]

$$\gamma = [Akg/(1+kL)]^{1/2} - \beta k v_a , \qquad (1)$$

whose parameters have been determined by comparing with simulations. Here A is the Atwood number, $k=2\pi/\lambda$, L is the density gradient scale length ($L = \rho/\nabla\rho$), v_a is the ablation velocity [$v_a = \dot{m}/(\rho \cdot \text{Area})$], and β is a multiplier between 1 and 2 for our indirect-drive experiments. The combination of slightly larger ablation velocity and gentler density gradient at the ablation front (larger L) for CH(Br) leads to a lower overall growth rate and a higher cutoff wavelength as compared to FS. For reference we also show the expected classical growth rate for ideal, incompressible fluids. The departure from classical for ablative growth is quite dramatic, especially at short wavelengths. Note that the details of this dispersion curve can actually be controlled by modifying the amount and type of dopants in the foils.

IV. MULTI-MODE EXPERIMENTS

When multiple modes are present in an initial perturbation, the behavior in the nonlinear regime is much more complex than for single modes. In addition to the bubble-and-spike formation described above, there is coupling between modes, say, k_i and k_j, to spawn new modes of wavenumber $k_i \pm k_j$. In the case of classical RT growth of incompressible fluids, the effect of this coupling is quite dramatic in that the modal structure of a perturbation late in time is completely dominated by mode coupling and bears no resemblance to the initial conditions.[27] This situation would be disastrous for ICF because developing smoother capsule surfaces and smoother laser beams would then not necessarily translate to less RT-induced mix in implosions. As we pointed out in Fig. 4d, however, perturbation growth at an ablation front does not at all resemble that of ideal incompressible fluids. It is quite critical, then, that we quantify exactly how mode coupling does behave at the ablation front. Theoretical estimates indicate that implosion performance is in fact sensitive to the initial conditions.[28] Other theoretical work suggests that the growth of one mode may be substantially altered by the presence of another.[29] Experiments are in order.

We begin with a discussion of our 2-mode (2λ) experiments, illustrated with the streaked image shown in Fig. 5a. The mold used to impose the initial 2λ perturbation on a CH(Br) foil is shown in Fig. 5b: $\lambda_{1,2}$ = 50, 75 μm with η_0 = 2 μm for each. A typical optical depth modulation profile is also shown. The Fourier coefficients for the two pre-existing modes, $\lambda_{1,2}$ = 50, 75 μm, are shown as a function of time in Fig. 5c. The Fourier coefficients for the $k_1 \pm k_2$ coupled modes, corresponding to wavelengths of 30 μm and 150 μm, are observed only after the RT instability has entered the nonlinear regime, as shown in Fig. 5d. The solid curves correspond to the LASNEX simulations of the 2λ experiment, and are

in reasonably good agreement with the data. We also show with the dashed curves in Fig. 5c the result we would have expected if only the λ = 75 μm or the λ = 50 μm perturbation had been present alone, based on the simulations. It is evident that in the nonlinear regime of the 2λ case, the evolution of mode k_1 is affected by the presence of mode k_2, and vice versa. We emphasize, however, that the overall perturbation growth is not necessarily retarded, but rather redistributed into a broader Fourier spectrum corresponding to a stronger change of shape due to the mode coupling.

We turn next to our 8-mode (8λ) experiments, as illustrated by the streaked image shown in Fig. 6a. The mold and a sample modulated optical depth profile late in time are shown in Fig. 6b. The initial perturbation was defined by λ_k = (180 μm)/k, k=1-8, and the amplitudes, η_k, were chosen at random and are given in the figure caption. The phases were chosen to maintain cosine symmetry, so that 2D simulations would be straightforward. In Fig. 6c we show the Fourier analysis of the data, overlaid with the simulations. Early in time during the linear regime, each mode grows at its own growth rate, (given by, say, Eq. 1) unaware of the presence of other modes. Late in time at 4.1 ns, however, the situation is quite different. The perturbation is dominated by modes k_3 and k_4, corresponding to λ = 60 μm and 45 μm, respectively, but the $k_4 \pm k_3$ modes (corresponding to λ = 180 μm and 25.7 μm) are also becoming quite prominent. The $2k_3$ mode, namely, the second harmonic of the λ = 60 μm mode, is also becoming reasonably strong. The simulations are in very good qualitative agreement, though the overall growth is overpredicted by ~30% late in time. We will be examining in the near future precisely how the modal spectrum shown at the top of Fig. 6c differs from that which would occur if each initial mode were allowed to grow alone, especially regarding saturation.

V. SURFACE-FINISH EXPERIMENTS

The only conclusive test of how a perturbation consisting of a full continuum of modes evolves at the ablation front is to actually impose such a perturbation and measure its evolution. We are just now starting such surface-finish experiments, as illustrated by the gated images shown in Fig. 7a. The CH(Br) foil had a rough surface of characteristic perturbation $\langle\eta_o\rangle \approx 2\pm1$ μm imposed on it. It is evident directly from the image that late in time the surface has evolved into large, roughly hexagonal bubbles of size ~100 μm. This is quantified by the optical depth (OD) modulation profiles shown in Fig. 7b. The peak-to-valley maximum δOD late in time (4.4 ns) of the largest bubble-and-spike feature is $\delta OD \approx 1.5$, which exceeds the original optical depth, OD_o, of the entire foil. For comparison, we show in Fig. 7c similar optical depth profiles for a smooth foil of characteristic surface roughness $\langle\eta_o\rangle \approx 3.5$ nm. There is no obvious growth into bubbles and spikes. Adopting an operational definition of foil "break up" as occurring when $\delta OD > OD_o$, we conclude that our nominal smooth foils remain intact throughout whereas foils imposed with a very rough initial surface finish break up late in time. The Fourier transforms corresponding to the optical depth profiles of Figs. 7b,c are given in Figs. 7d,e. For the rough surface, the growth late in time is dominated by modes k = 3-8 corresponding to $\lambda \approx$ 150-50 μm. The Fourier data for the smooth foil show no significant growth. We are currently in the process of doing more detailed characterization of the surface finishes, after which we will examine in depth the coupling and saturation effects for this broad spectrum of initial modes.

VI. CONCLUSION AND SUMMARY

In conclusion, we have done an extensive series of experiments accelerating FS foils and CH(Br) foils by x-ray ablation using a shaped, low

adiabat drive. The RT-induced perturbation growth was studied by imposing single-mode and multi-mode sinusoidal initial perturbations, and also by accelerating a foil with a rough surface finish. We use our single-mode experiments along with foil trajectory experiments to develop a modeling capability that reliably reproduces observation, then use the simulations to illustrate the subtle differences in behavior between FS and CH(Br) foils, with the latter being slightly less RT unstable. Clear evidence of mode coupling is seen in the multi-mode experiments, with the $k_i \pm k_j$ coupled modes being spawned in the nonlinear regime. The agreement with simulations for the coupling experiments is very good as well, allowing us to then use the model to predict what we would have seen if each mode were allowed to grow individually. Mode coupling leads to a substantial change in shape of the perturbation, resulting in a general broadening of the Fourier spectrum. Very recent surface finish experiments show that smooth foils remain intact whereas foils with a very rough surface finish break up. We will be examining in the near future the details of exactly how multiple modes evolve differently than single modes, with particular attention paid to saturation effects.

It is a pleasure to acknowledge the dedicated staff and support personnel at Nova. This work was performed under the auspices of the U.S. DOE by the Lawrence Livermore National Laboratory under contract number W-7405-ENG-48.

References:

[1]S. Chandrasekhar, *Hydrodynamic and Hydromagnetic Stability* (Oxford U.P., London, 1968), Chap. 10; Lord Rayleigh, *Theory of Sound*, 2nd ed. Vol. 2 (Dover, New York, 1945); *ibid*, Proc. London Math. Soc. **10**, 4 (1879); reprinted in Scientific Papers, Vol. I (Cambridge Univ. Press, Cambridge, England, 1899), p. 361; *ibid*, Proc. London Math. Soc. **14**, 170 (1883); reprinted in Scientific Papers, Vol. II (Cambridge Univ. Press, Cambridge, England, 1900), p. 200; G.I. Taylor, Proc. Roy. Soc. **A201**, 192 (1950).

[2]D.H. Sharp, Physica D **12**,3 (1984).

[3]Lord Kelvin, *Hydrodynamics and General Dynamics* (Cambridge University Press, Cambridge, 1910), pp. 69ff; H. Helmholtz, Philos. Mag., Ser. 4, **36**, 337 (1868); B.J. Daly, Phys. Fluids **10**, 297 (1967); A. Ferrari, E. Trussoni, and L. Zaninetti, Mon. Not. R. astr. Soc. **196**, 1051 (1981); S. Parhi, Phys. Fluids B 4, 1589 (1992).

[4]R.D. Richtmyer, Commun. Pure Appl. Math. **13**, 297 (1960); E.E. Meshkov, Izv. Akad. Nauk. SSSR, Mekh. Zhidk. Gaz. **5**, 151 (1969) (NASA TTF-13-074, 1970); K.O. Mikaelian, Phys. Fluids A **3**, 2638 (1991); L.D. Cloutman and M.F. Wehner, LLNL Report UCLR-JC-108795, in press, Phys. Fluids A (1992).

[5]T. Ebisuzake, T. Shigeyama, and K. Nomoto, Astro. J. **344**, L65 (1989); T. Shigeyama, K. Nomoto, and M. Hashimoto, Astron. Astrophys. **196**, 141 (1988); L. Smarr, J.R. Wilson, R.T. Barton, and R.L. Bowers, As. J. **246**, 515 (1981); B. Fryxell, E. Müller, and D. Arnett, As. J. **367**, 619 (1991).

[6]J. Arons and S.M. Lea. As. J. **207**, 914 (1976); R.F. Elsner and F.K. Lamb, As. J. 215, **897** (1977); Y-M. Wang and M. Nepven, Astron. and Astrophysics **118**, 267 (1983).

[7]F. Cattaneo and D.W. Hughes, J. Fluid Mech. **196**, 323 (1988).

[8]L.G. Moretto, K. Tso, N. Colonna, and G.J. Wozniak, Phys. Rev. Lett. **69**, 1884 (1992).

[9]S.V. Sazonov, Planet. Space Sci. 39, 1667 (1991).

[10]P.A. Bernhardt, R.A. Roussel-Dupre, M.B. Pongratz, G. Haerendel, A. Valenzuela, D.A. Gurnett, and R.R. Anderson, J. Geophys. Res. **92**, 5777 (1987).

[11]W.S.D. Wilcock and J.A. Whitehead, J. Geophys. Res. **96**, 12193 (1991).

[12]A.B. Bud'ko, M.A. Liberman, A.L Velikovich, and F.S. Felber, Phys. Fluids B **2**, 1159 (1990).

[13]J.M. Finn, Bull. Am. Phys. Soc. **37**, 1544 (1992, Abstract 7R19).

[14]M.N. Rosenbluth and C.L. Longmire, Ann. Phys. 1, 120 (1957); H. Dickinson, W.H. Bostick, J.N. DiMarco, and S. Koslov, Phys. Fluids 5, 1048 (1962); B.H. Ripin, E.A. McLean, C.K. Manka, C. Pawley, J.A. Stamper, T.A. Peyser, A.N. Mostovych, J. Grun, A.B. Hassam, and J. Huba, Phys. Rev. Lett. **59**, 2299 (1987); A.L. Velikovich, Phys. Fluids B **3**, 492 (1991).

[15]J.D. Lindl and W.C. Mead, Phys. Rev. Lett. **34**, 1273 (1975); H. Sakagami and K. Hishihara, Phys. Fluids B **2**, 2715 (1990).

[16]J. Grun, M.E. Emery, C.K. Manka, T.N. Lee, E.A. McLean, A. Mostovych, J. Stamper, S. Bodner, S.P. Obenshain, and B.H. Ripin, Phys. Rev. Lett. **58**, 2672 (1987); M. Desselberger, O. Willi, M. Savage, and M. Lamb, Phys. Rev. Lett. **65**, 2997 (1990); S.G. Glendinning, S.V. Weber, P. Bell, L.B. DaSilva, S.N. Dixit, M.A. Henesian, D.R. Kania, J.D. Kilkenny, H.T. Powell, R.J. Wallace, P.J. Wegner, J.P. Knauer, and C.P. Verdon, Phys. Rev. Lett. **69**, 1201 (1992).

[17]B.A. Remington, S.W. Haan, S.G. Glendinning, J.D. Kilkenny, D.H. Munro, and R. Wallace, Phys. Rev. Lett. **67**, 3259 (1991); *ibid*, Phys. Fluids B **4**, 967 (1992); B.A. Remington, S.W. Haan, S.G. Glendinning, J.D. Kilkenny, and R. Wallace, proceedings of the *3rd International Workshop on the Physics of Compressible Turbulent Mixing*, Abbey of Royaumont, France (CEA DAM), 225 (1992); J.D. Kilkenny, Phys. Fluids B **2**, 1400 (1990).

[18]R.J. Ellis, J.E. Trebes, D.W. Phillion, J.D. Kilkenny, S.G. Glendinning, J.D. Wiedwald, and R.A. Levesque, Rev. Sci. Instrum. **61**, 2759 (1990) and references therein; B.A. Remington, S.G. Glendinning, R.J. Wallace, S. Rothman, R. Morales, Rev. Sci. Instrum. **63**, 5080 (1992).

[19]B.A. Remington, B.A. Hammel, O.L. Landen, and R.A. Pasha, Rev. Sci. Instrum., Rev. Sci. Instrum. **63**, 5083 (1992); B.A. Hammel, D. Griswold, N. Landen, T. Perry, B. Remington, J.D. Kilkenny, and R. Pasha, UCRL-JC-111933, subitted to J. Applied Phys. (1992).

[20]P.M. Bell, J.D. Kilkenny, O.L. Landen, R.L. Hanks, and D.K. Bradley, Rev. Sci. Instrum **63**, 5073 (1992); J. Oertel, B. Watt, T. Archuleta, J. Jimerson, J. Wiedwald, P. Bell, and R. Hanks, bull. Am. Phys. Soc. **37**, 1522 (1992).

[21]E.M. Campbell, Laser and Part. Beams **9**, 209 (1991); E.M. Campbell, J.T. Hunt, E.S. Bliss, D.R. Speck, and R.P. Drake, Rev. Sci. Instrum. **57**, 2101 (1986).

[22]G.B. Zimmerman and W.L. Kruer, Comments Plasma Phys. Controlled Fusion **11**, 51 (1975).

[23]D. Layzer, As. J. **122**, 1 (1955).

[24]A. Bar-Shalom, J. Oreg, W.H. Goldstein, D. Shvarts, and A. Zigler, Phys. Rev. A **40**, 3183 (1989); A. Bar-Shalom, J. Oreg, and W.H. Goldstein, UCRL-JC-

105957 (1991) and in *Radiative Processes of Hot Dense Matter*, Ed. by W. Goldstein et al. (World Scientific, New Jersey, 1991), p. 163.

[25]C.A. Iglesias, F.J. Rogers, and B.G. Wilson, Ap. J. **397**, 717 (1992); *ibid* **360**, 221 (1990); *ibid* **322**, L45 (1987); F.J. Rogers and C.A. Iglesias, Ap. J. Suppl. **79**, 507 (1992).

[26]H. Takabe, L. Montierth, and R.L. Morse, Phys. Fluids 26,2299 (1983); H. Takabe, K. Mima, L. Montierth, and R.L. Morse, ibid **28**, 3676 (1985); D.H. Munro, Phys. Rev. A **38**, 1433 (1988).

[27]D.L. Youngs, Phys. Fluids A **3**, 1312 (1991).

[28]S.W. Haan, Phys. Rev. A **39**, 5812 (1989); *ibid*, Phys. Fluids B **3**, 2349 (1991).

[29]J.P. Dahlburg, J.H. Gardner, and M.H. Emery, Bull. Am. Phys. Soc. **35**, 1969 (1990, Abstract 3E3); D. Ofer, D. Shvarts, Z. Zinamon, S.A. Orszag, Phys. Fluids B **4**, 3549 (1992).

Figure Captions:

Figure 1. Setup for indirect-drive Rayleigh-Taylor experiments. (a) Schematic of the experimental setup (not to scale). The foil is mounted on the front wall of a cylindrical gold hohlraum with surface perturbation facing inwards, and drive beams entering the ends of the hohlraum generate an approximately thermal x-ray drive. A separate laser beam striking a backlighter disk generates a back illumination of x-rays at higher frequency but much lower flux. (b) The solid curves give the power versus time of the eight 1/3 μm drive laser beams. The dotted curve gives the power and relative timing of the 1/2 μm backlighter beam. (c) Typical image of a streaked foil trajectory measurement. (d) Analyzed result of three such trajectory shots, along with the result of a 1D LASNEX simulation.

Figure 2. Results of a side-on perturbation growth experiment using an gated, x-ray pinhole imager as the diagnostic. (a) The ablation front corresponds to the lower side of the foil. The images are separated vertically according to the striplines in the diagnostic, with times set independently to 2.0, 3.2, and 4.4 ns. Horizontally, the images are separated in time by only ~60 ps, corresponding to the finite transit time of the HV pulse traveling down the stripline. The images are also offset spatially by parallax, leading to a stereoscopic view of the foil. (b) Blowup of the bottom right image, compared with (c) a contour plot from 2D LASNEX simulations.

Figure 3. Typical example of a measurement of perturbation growth using face-on radiography. (a) Streaked image for a CH(Br) foil with a λ = 100 μm, η_0=2.5 μm perturbation. (b) The corresponding modulated optical depth profiles at three different times spanning the linear and nonlinear regimes. (c) Fourier decomposition of the profiles shown in (b) showing that the

shape change in the nonlinear regime is reflected by the generation of higher harmonics, in this case the first 5 harmonics.

Figure 4. Face-on measurements of growth in the linear regime. (a) Streaked image of a FS foil with a λ = 50 μm, η_o=0.8 μm perturbation. (b) Coefficients of the fundamental mode for the FS image shown in (a). (c) Same only for a CH(Br) foil with a λ = 50 μm, η_o = 0.5 μm initial perturbation. The smooth curves are the results of 2D LASNEX simulations, including the effect of the instrument MTF. The starting time, t=0, corresponds to the start of the drive lasers. (d) Fitting a simple dispersion relation to results of the simulation for very small η_o perturbations, we then can plot for a given acceleration, g = 60 μm/ns^2, the growth rate versus λ for the two foil materials, as compared to the classical result. The effect of ablation is to cause a short-λ cutoff, with the cutoff occurring at a larger λ for CH(Br) compared to FS.

Figure 5. Results of 2-mode (2λ) experiments and simulations. (a) Streaked image for a 2λ foil with λ_1, λ_2 = 50, 75 μm, η_o=2.0 μm (b) Mold used in making the foils, and a typical contrast profile from (a). (c) Fourier coefficients of the two pre-existing modes, compared with the results of 2D LASNEX simulations for the 2λ case (solid curves) versus calculations where either the λ = 50 μm perturbation or the λ = 75 μm perturbation were present alone, "1λ calc" (dashed curves). (d) The two coupled modes are shown along with the results of the simulations (solid curves).

Figure 6. Results of 8-mode (8λ) experiments and simulations. (a) Streaked image for an 8λ foil with λ = (180 μm)/k, k=1,8 and $\eta_{1\text{-}8}$ = 0.31, -0.30, 0.36, -0.37, -0.28, 0.21, -0.17, and -0.07 μm, respectively. (b) Profile of the mold is shown along with a typical profile of contrast. (c) The Fourier decomposition of the growing perturbation is shown at four different times

(solid histogram) along with the results of the 2D LASNEX simulation (dotted curve).

Figure 7. Results of surface-finish experiments. (a) Gated x-ray framing images of a backlit, accelerated foil with a very rough surface. (b) Corresponding optical depth profiles for the data shown in (a). (c) Same as (b) except for a smooth foil. (d) Fourier decomposition of the optical depth profiles shown in (b). (e) Same as (d) except for the smooth foil.

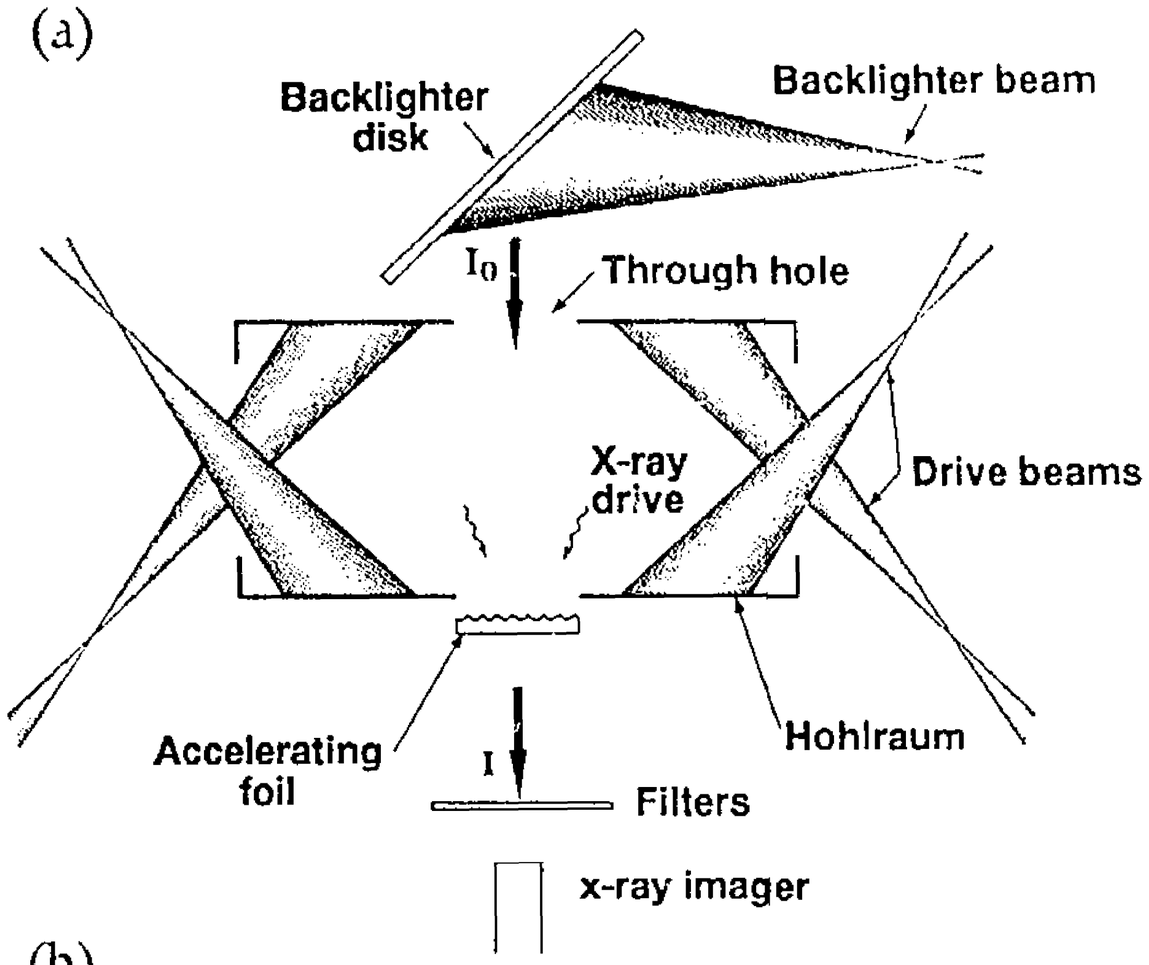
(a)
Backlighter disk
Backlighter beam
I_0
Through hole
X-ray drive
Drive beams
Accelerating foil
I
Hohlraum
Filters
x-ray imager

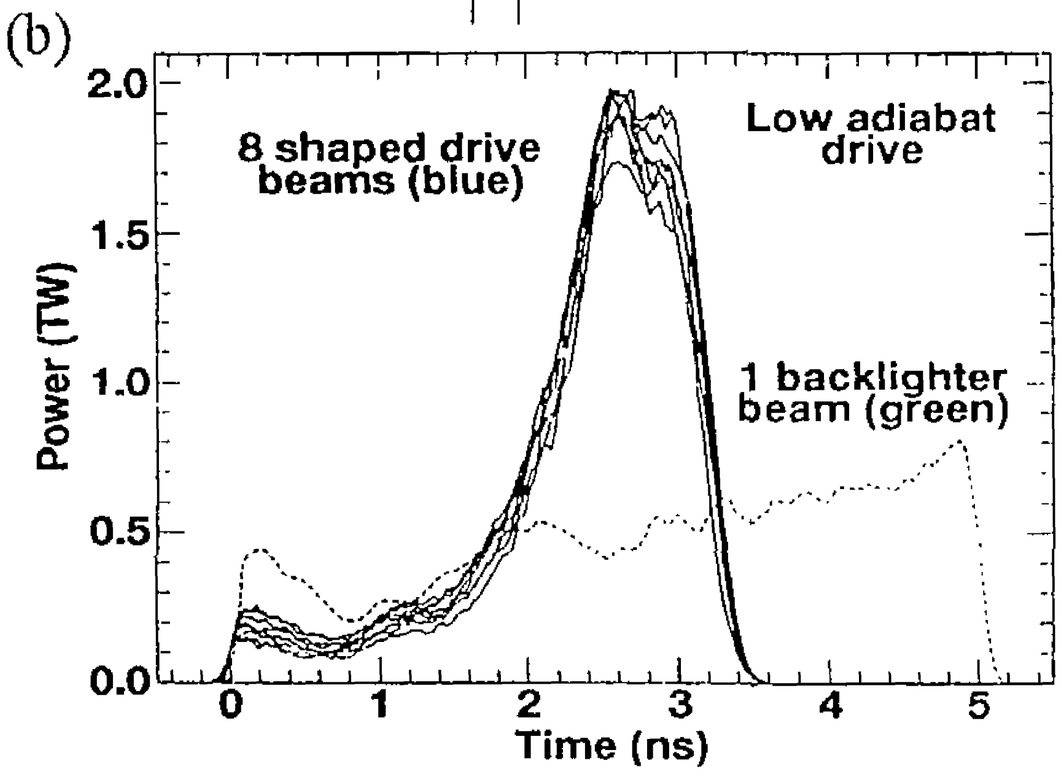
(b)
8 shaped drive beams (blue)
Low adiabat drive
1 backlighter beam (green)
Power (TW)
Time (ns)

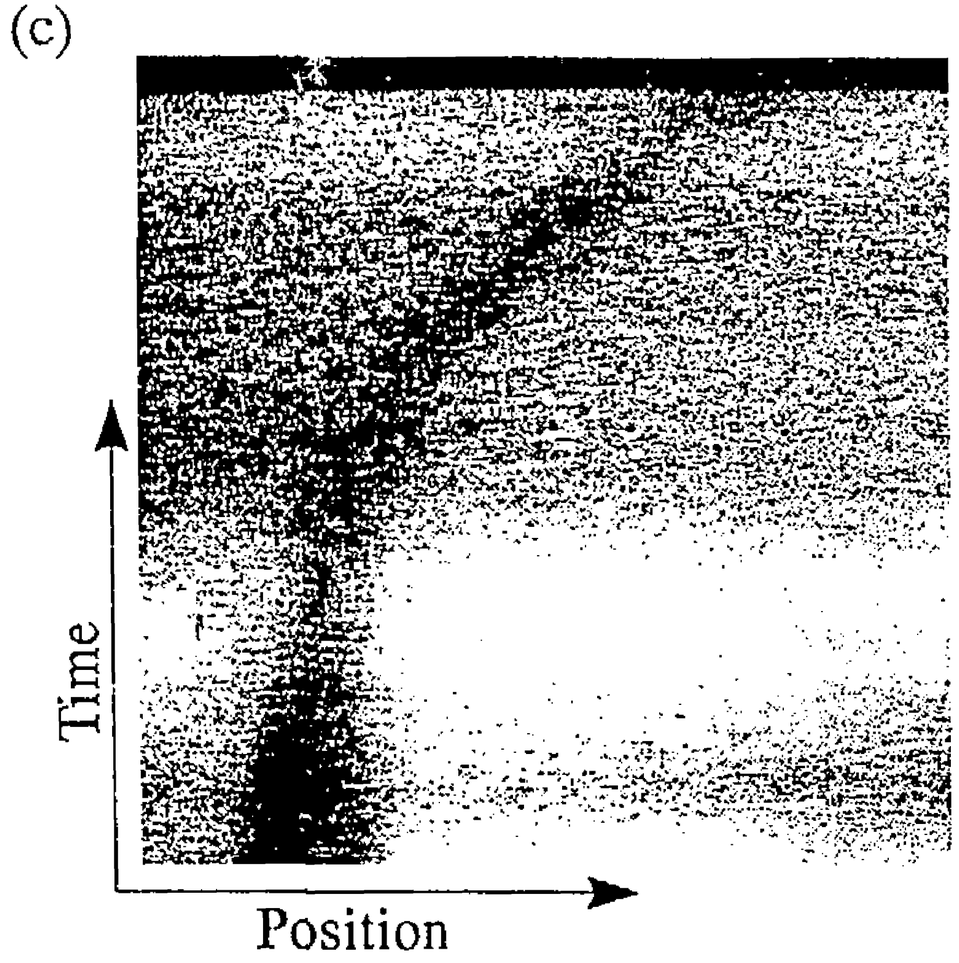
(c)
Time
Position

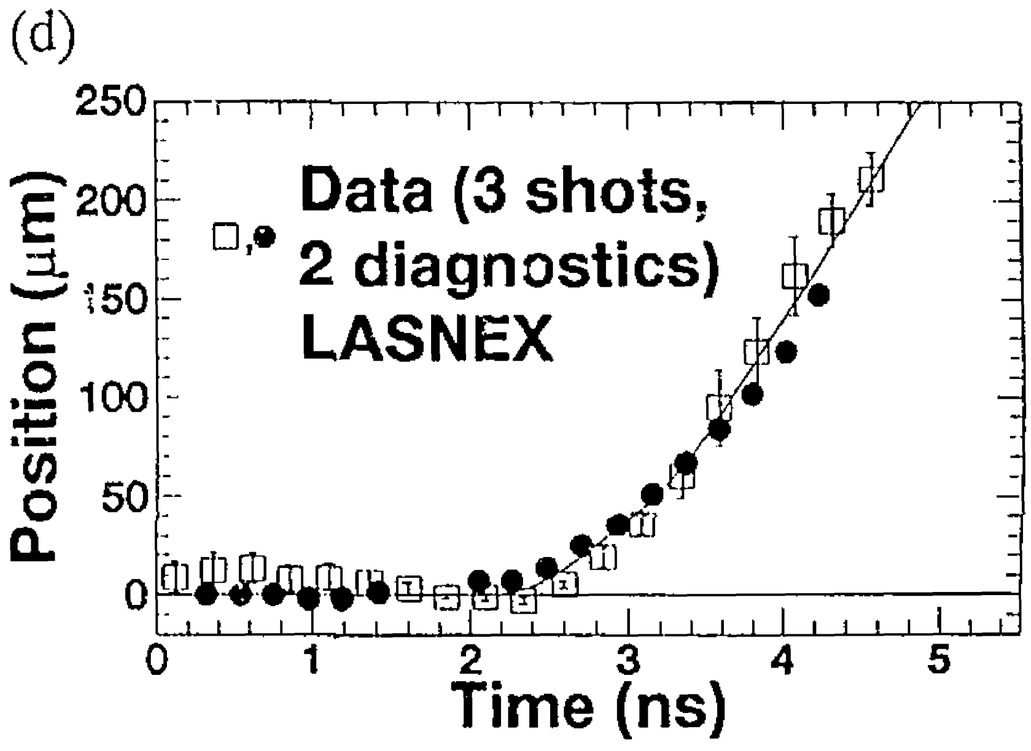
(d)
Data (3 shots, 2 diagnostics)
LASNEX
Position (μm)
Time (ns)

Figure 1

(a)

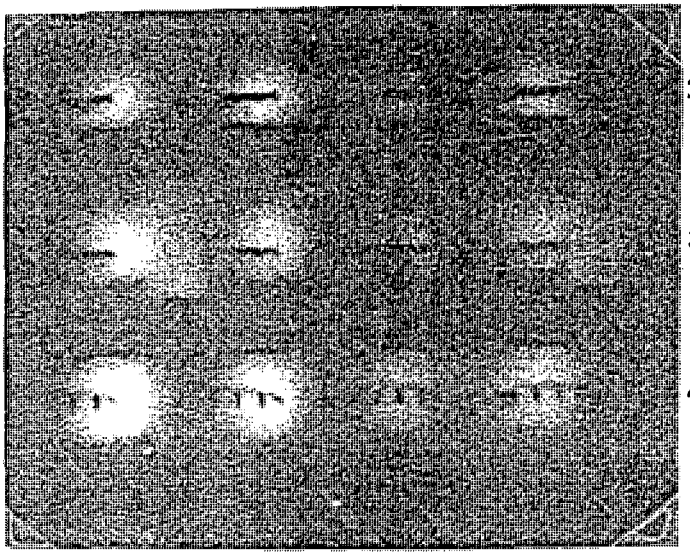

(b)

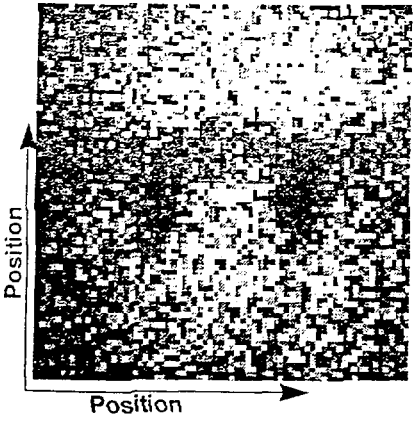

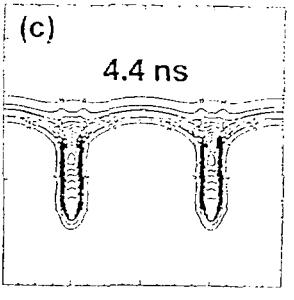

Figure 2

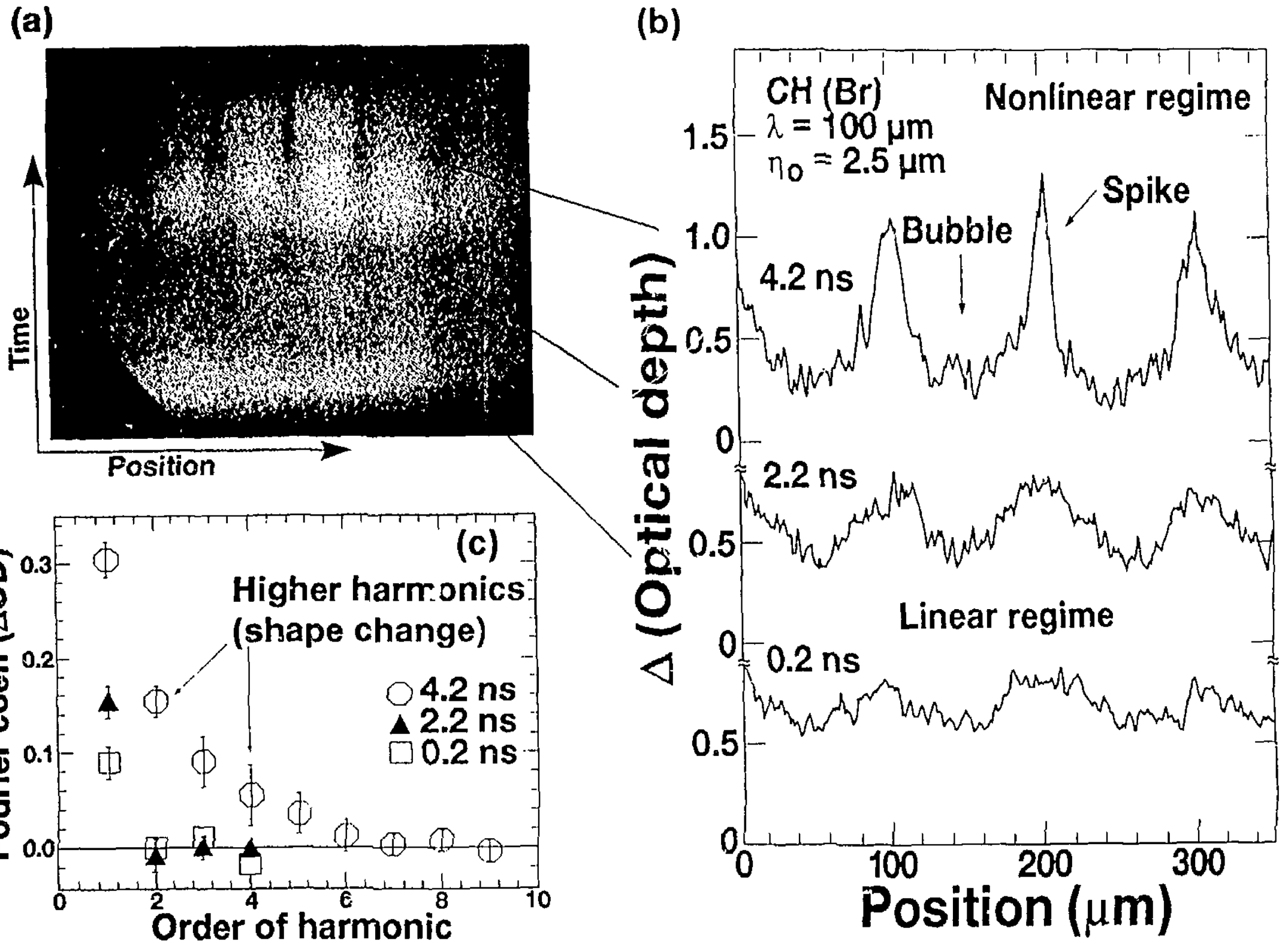
(a)
Time
Position
(b)
CH (Br)
λ = 100 μm
η0 ≈ 2.5 μm
Nonlinear regime
Spike
Bubble
4.2 ns
2.2 ns
Linear regime
0.2 ns
Δ (Optical depth)
Position (μm)
(c)
Higher harmonics
(shape change)
4.2 ns
2.2 ns
0.2 ns
Fourier coeff (ΔOD)
Order of harmonic

Figure 3

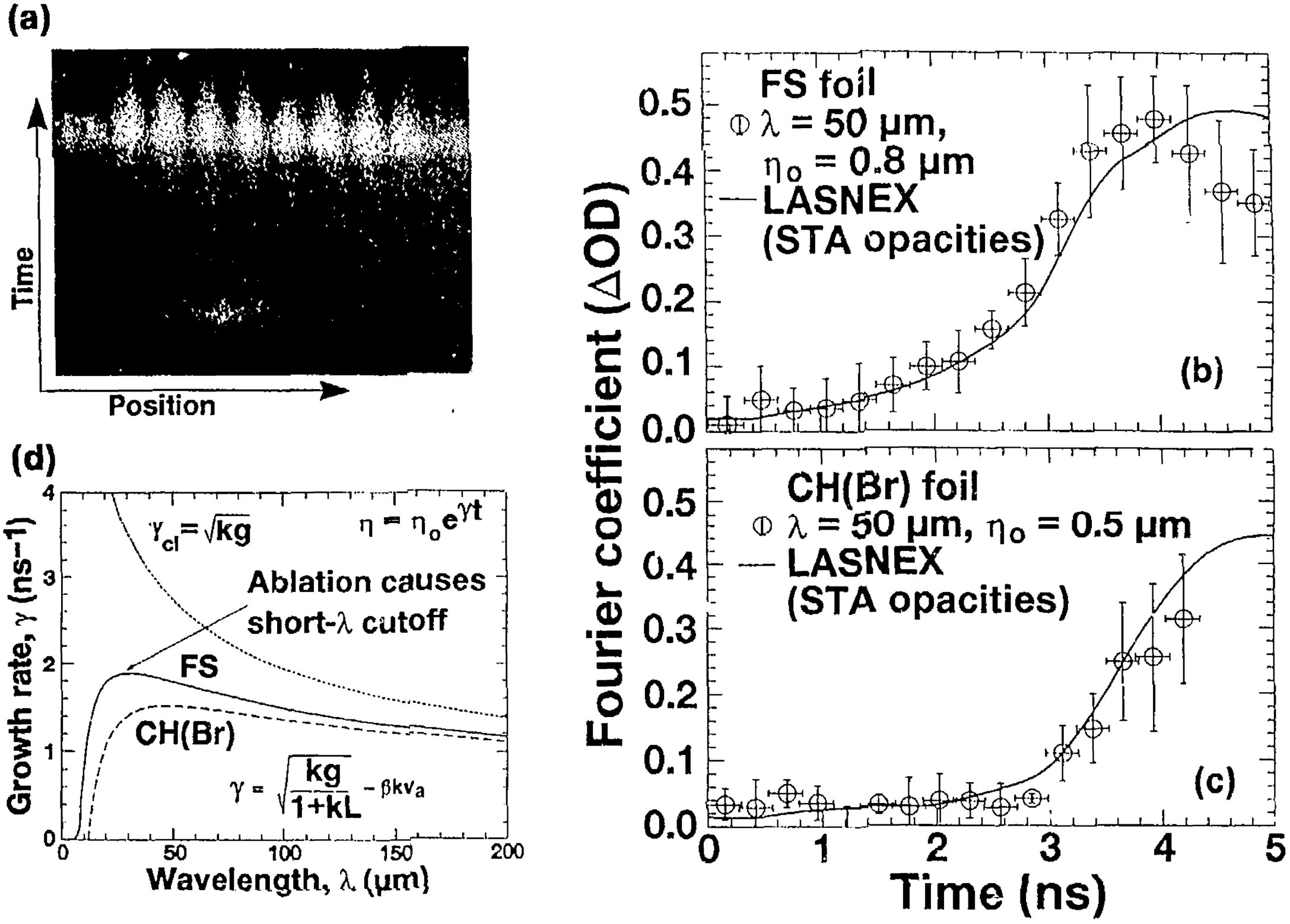
(a)
Time
Position
(d)
Growth rate, γ (ns⁻¹)
Wavelength, λ (μm)
γ_cl = √kg
η = η_o e^γt
Ablation causes
short-λ cutoff
FS
CH(Br)
γ = √(kg/(1+kL)) − βkv_a
0
1
2
3
4
0
50
100
150
200
FS foil
Φ λ = 50 μm,
η_o = 0.8 μm
LASNEX
(STA opacities)
(b)
CH(Br) foil
Φ λ = 50 μm, η_o = 0.5 μm
LASNEX
(STA opacities)
(c)
Fourier coefficient (ΔOD)
0.0
0.1
0.2
0.3
0.4
0.5
0
1
2
3
4
5
Time (ns)

Figure 4

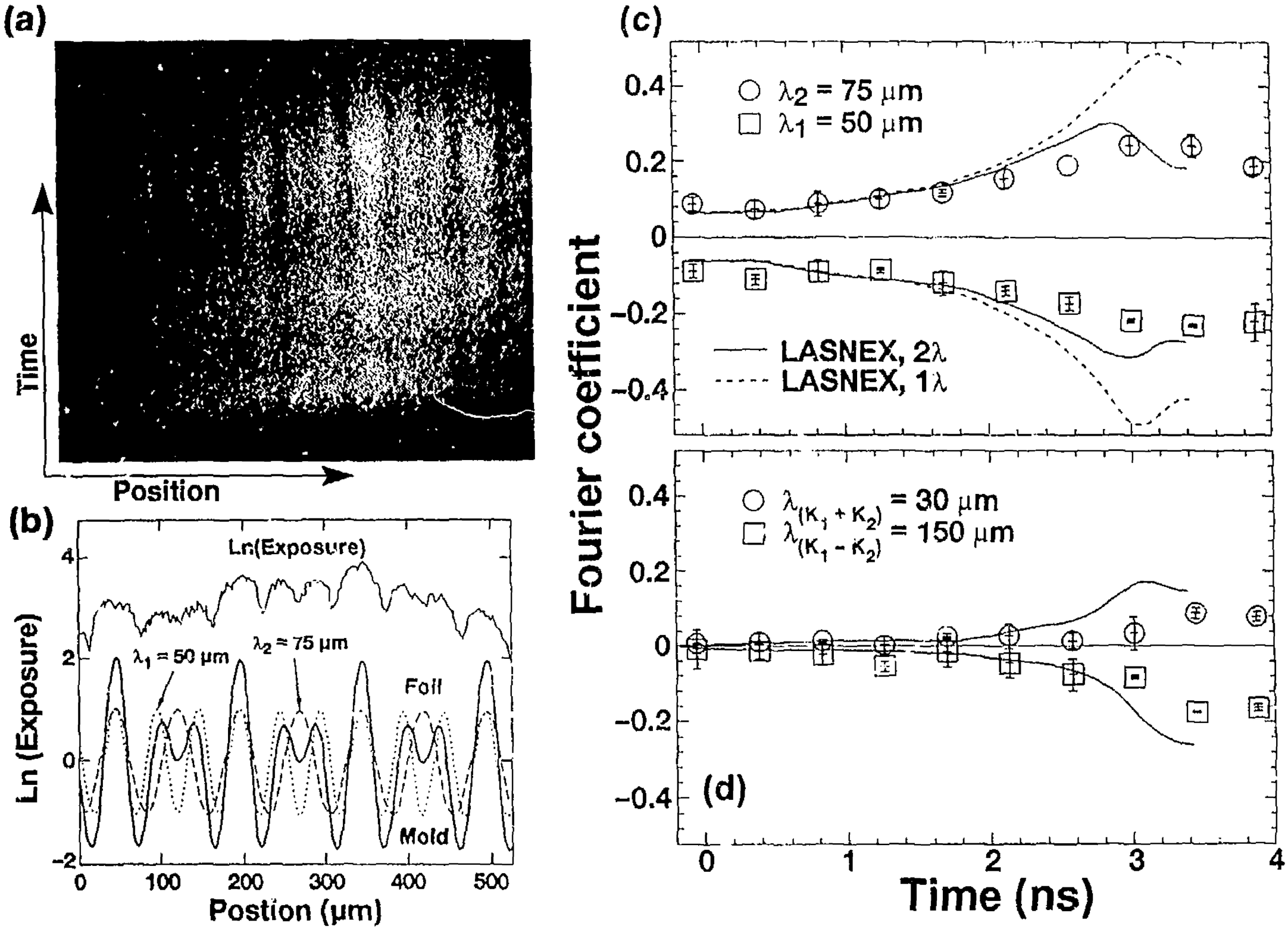
(a)
Time
Position
(b)
Ln(Exposure)
Ln (Exposure)
λ1 = 50 μm
λ2 = 75 μm
Foil
Mold
Postion (μm)
(c)
λ2 = 75 μm
λ1 = 50 μm
LASNEX, 2λ
LASNEX, 1λ
Fourier coefficient
λ(K1 + K2) = 30 μm
λ(K1 - K2) = 150 μm
(d)
Time (ns)

Figure 5

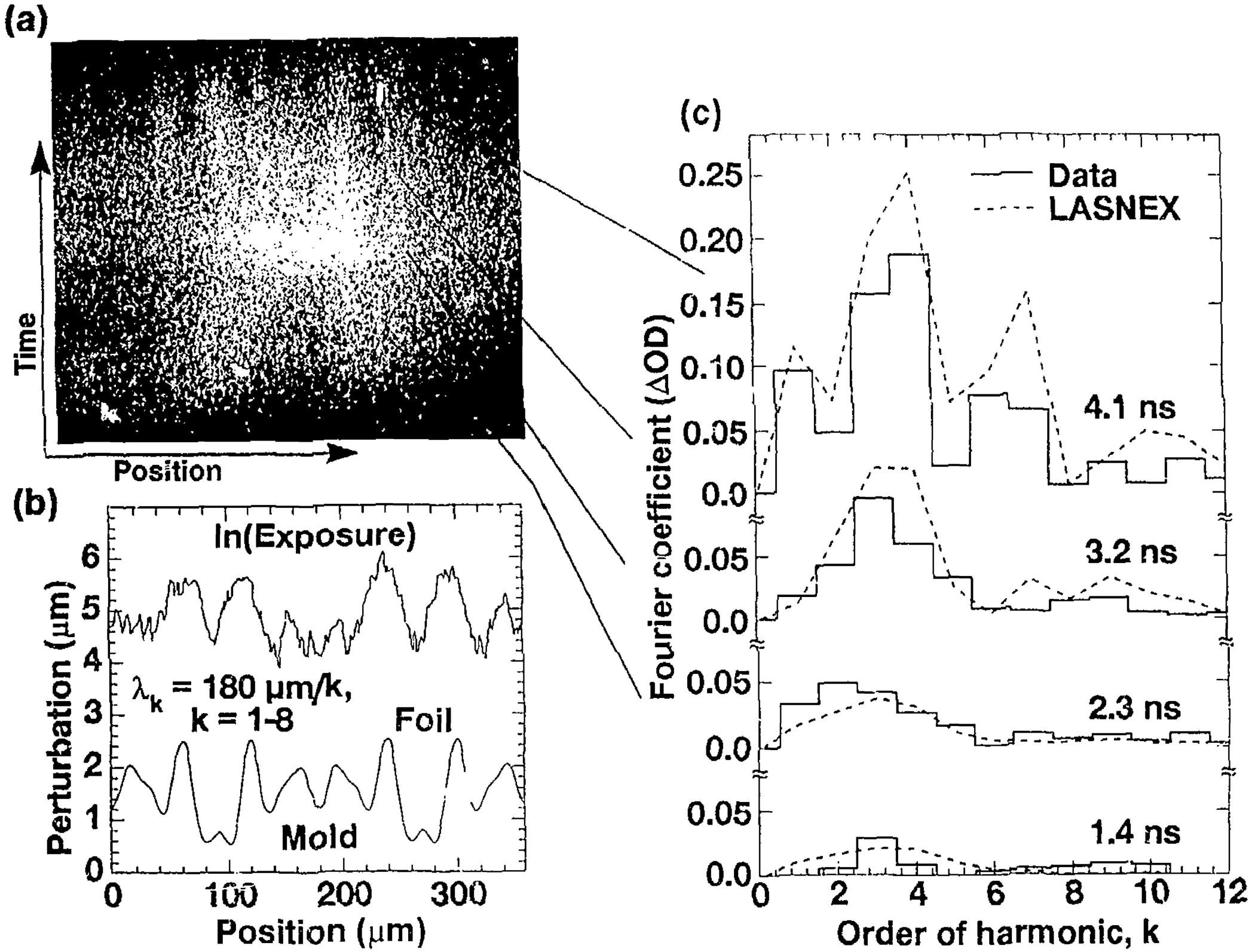
(a)
Time
Position
(b)
ln(Exposure)
Perturbation (μm)
λ_k = 180 μm/k,
k = 1-8
Foil
Mold
Position (μm)
(c)
Data
LASNEX
4.1 ns
3.2 ns
2.3 ns
1.4 ns
Fourier coefficient (ΔOD)
Order of harmonic, k

Figure 6

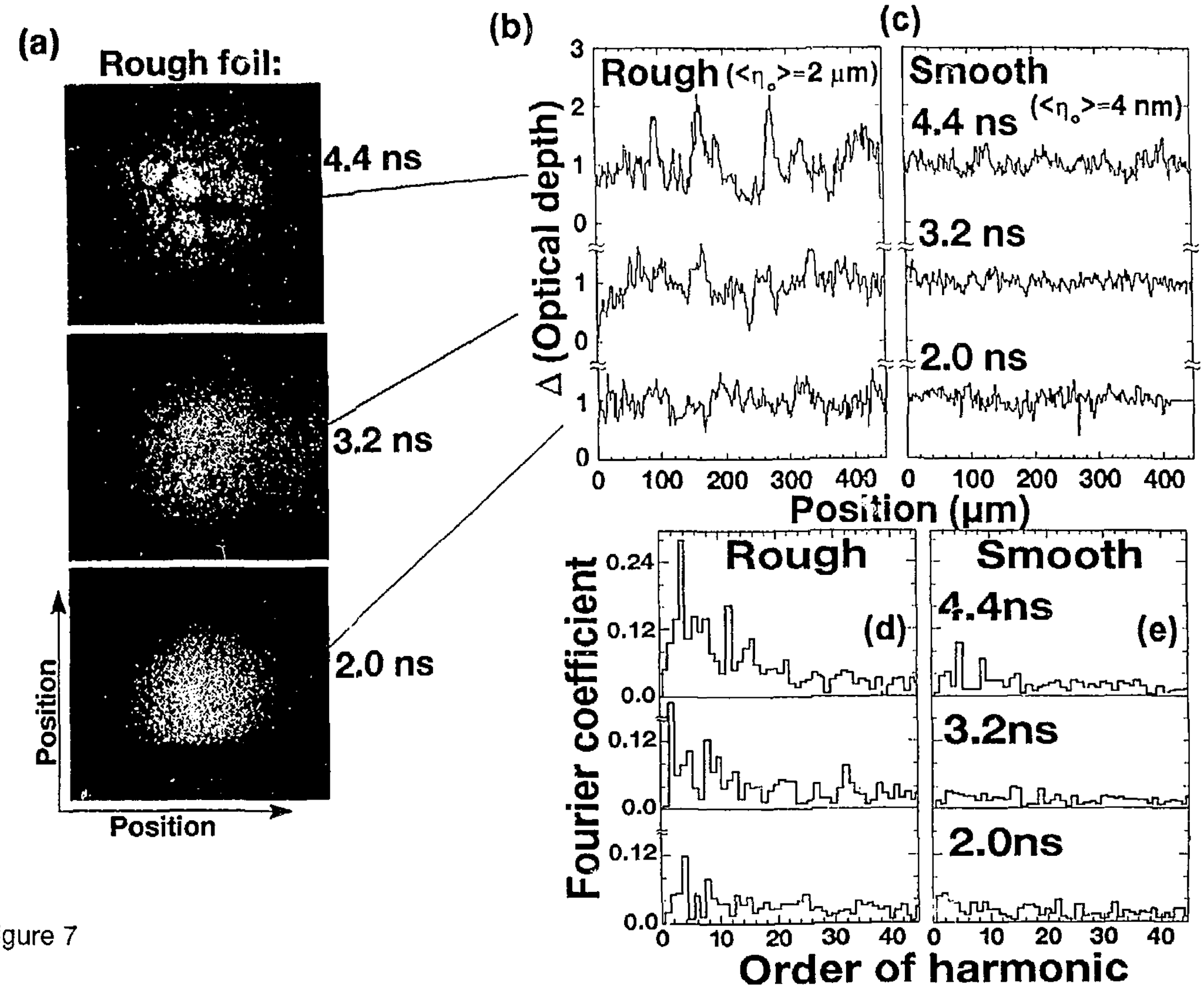
(a)
Rough foil:
4.4 ns
3.2 ns
2.0 ns
Position
Position
(b)
Rough (<η₀>=2 μm)
Δ (Optical depth)
3
2
1
0
1
0
1
0
0
100
200
300
400
(c)
Smooth
4.4 ns (<η₀>=4 nm)
3.2 ns
2.0 ns
0
100
200
300
400
Position (μm)
Rough
Smooth
Fourier coefficient
0.24
0.12
0.0
(d)
(e)
4.4ns
3.2ns
2.0ns
0
10
20
30
40
Order of harmonic

Figure 7